Investigation of Surface Roughness on the Transient Point of a Blunt Nose Cone

A Project Presented to
The Faculty of the Department of Aerospace Engineering
San Jose State University

In Partial Fulfillment to the Requirements of the Degree
Master of Science in Aerospace Engineering

By

Terrence Soares

Approved by

Dr. Periklis E. Papadopoulos
Faculty Advisor

©May 2020

Table of Contents

List of Figures

List of Tables

Abstract

This paper will demonstrate a parametric study on how the angle of a blunt cone and the varying external roughness of the cone affect the flow transition from laminar to turbulent. Conducted from 3D simulation, an analytical comparison is done of the wall temperatures of several nose cones when the surface roughness is altered. From these simulations, it is seen how the transition point changes with each simulation case. The comparative data enables an understanding of how different nose cones affect the performance of an applicable vehicle whether it be on Earth or in space. Nine cases will be simulated where the nose cone angle will be at 30, 45, and 60 degrees, each angle being tested with a roughness height of 0, 3, 5.6, and 10 μm.

Nomenclature

Symbols	Definition	Units
D	Diameter or length	m
L	Length	m
g	Gravity	m/s^2
M	Mach	m/s
P	Pressure	pa
q	slope	------
R	Length or radius	m
T	Temperature	K
V	Velocity	m/s
xa	Distance between cone tip and spherical edge	m
xo	Distance between cone tip and center of a sphere	m
xt	Tangency point	
x/L	Nose cone hypotenuse	m

Greek Symbols		
β	Shock angle	Degrees
∇	Gradient	------
∂,D	Partial derivation	------
ρ	Density	g/(cm)^3
θ	Theta of nose cone/ Wedge angle/ Expansion angle	Degrees
γ	Specific heat ratio	
μ	Dynamic viscosity	kg*m*s^-1
ν	Prandtl- Meyer angle	Degrees
Subscripts		
B	Base	------
C	Cone	------
N	Nose	------
Acronyms		
AM	Additive manufacturing	------
CAD	Computer-aided design	------
CNC	Computational numerical control	------
GH2	Gaseous hydrogen	------
K	Kelvin	------
LOX	Liquid oxygen	------
Re	Reynolds number	------

1. Introduction

1.1 Motivation

Aerodynamics plays a key role in how a vehicle will perform during flight. It demonstrates the principles around how a solid object will move through the air. Considering this, it makes sense to look at how surface roughness affects airflow, and thus vehicle performance. With companies using additive manufacturing to 3D print metal parts, they are starting to rely on machine accuracy[1] for complicated prints. Though this method saves time and money, it increases the risk of rough patches due to layering done by 3D printing. Known as the "stairing" method, depending on how the layers are set up in either term of thickness or number will affect the amount of roughness present when the printing is done[2].

The importance of this topic comes from how the degree of roughness will affect the transition point of laminar to turbulent flow. Turbulent flow is defined as a fluid characterized by chaotic changes in pressure and flow velocity[3], this is more evident with rougher surfaces. This, in turn, will affect how the nose cone should be designed and manufactured. Laminar flow tends to lower heat transfer quantity while turbulence does the opposite, so the various case simulations will give a better idea of how to move forward with design projects.

1.2 Literature review

1.2.1 Additive manufacturing

Additive Manufacturing(AM) is the process of joining materials to create objects from 3D models[4]. Looking at Figure 1.1, the various types of metallic additive techniques are presented.
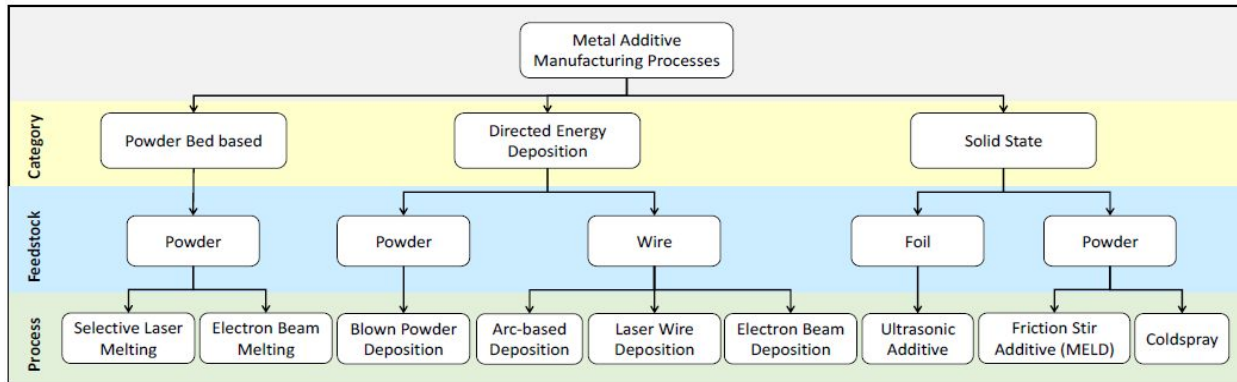
Figure 1.1 - Metallic additive techniques [4]

AM is broken up into three categories: power bed-based, directed energy deposition, and solid-state. Power bed processes are broken into Selective Laser Melting and Electron Beam Melting. In Figure 1.2, using a beam of a laser, layers of material are sintered and solidified. The advantage of this is that it allows for higher resolution products, enabling more complicated 3D model designs[4]. An extra advantage of Electron Beam is that it is performed under a vacuum, which is more suitable for more reactive materials[4].
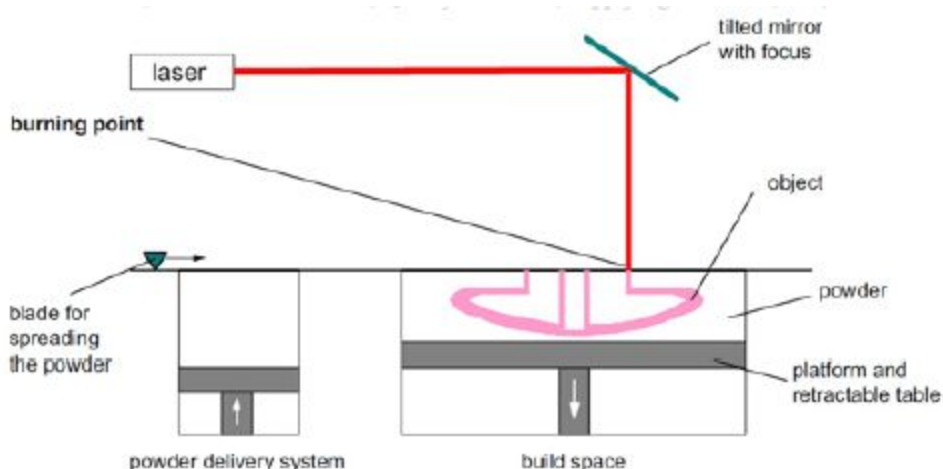
Figure 1.2 - Powder bed based manufacturing [4]

Directed Energy differs from power bed in that it also uses wire for a couple of its processes. It can be used as a replacement for casting or forging. Blown Powder Deposition which is the only directed energy process that uses powder differs from the powder bed method because it uses a melted pool to create layers, thus eliminating the need for sintering. Laser Wire Deposition uses a wire-fed melt pool to create more intricate designs such as cooling channels in a rocket nozzle as seen in Figure 1.4. Arc-Based Deposition uses a metal inert gas welding process for net shapes

while Electron Beam Deposition uses an electron beam as an energy source in a vacuum for wire-fed deposition.

Figure 1.3 - Blown powder deposition [4]
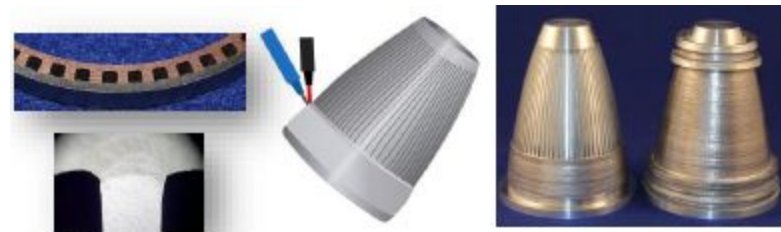
Figure 1.4 - Laser wire deposition [4]

Figure 1.5 - Arc-based deposition [4]

Figure 1.6 - Electron beam deposition [4]

Solid State Manufacturing is a hybrid of AM and traditional manufacturing. Ultrasonic Additive involves the ultrasonic welding of foil layers run through a CNC (Computational Numerical Control) machine[5]. In Figure 1.7 - 1.9, the step process is shown in how the metal foil is put under heat and pressure to form shapes. Friction Stir Additive involves using a rotating pin to

create friction and heat that in turn causes the material to weld together. Cold Spray uses pressurized gas to pact material together rather than sintering.
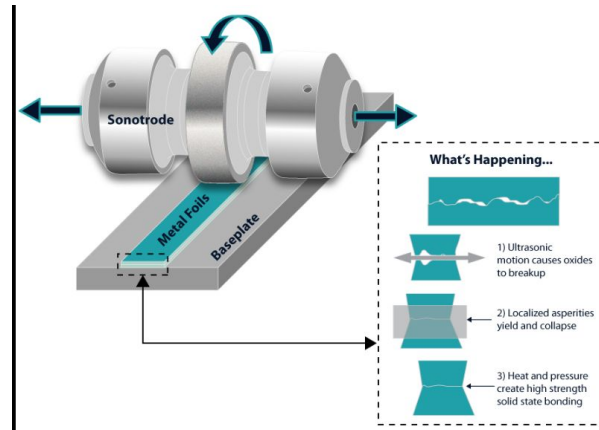
Figure 1.7 - Ultrasonic additive [5]
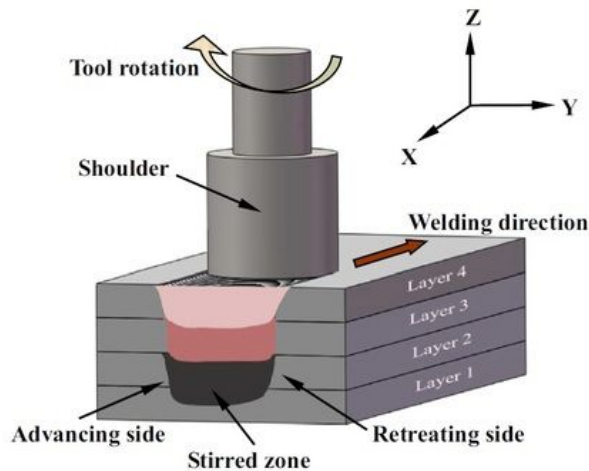
Figure 1.8 - Friction stir additive [6]
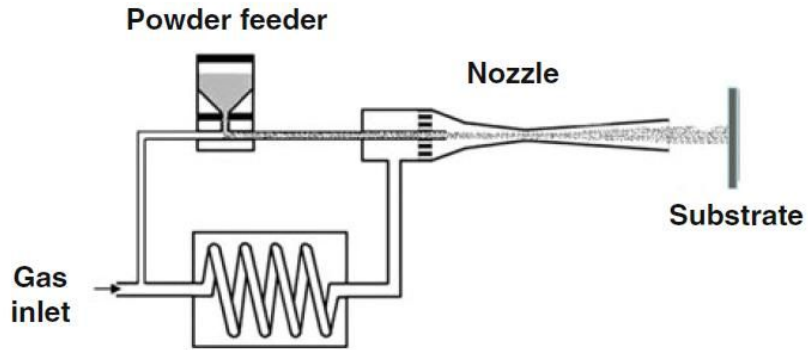
Figure 1.9 - Cold spray [7]

In a journal article titled "*Additive Manufacturing Development and Hot-fire Testing of Liquid Rocket Channel Wall Nozzles using Blown Powder Directed Energy Deposition Inconel 625 and JBK-75 Alloys*" written by Paul R Gradl and associates, Gradl starts off by going into detail how AM is being used as an alternate fabrication technique to create complex geometries for engine components at low costs. Focusing on powder bed fusion - selective laser melting and directed energy deposition, the nozzles are designed with coolant channels and hot fire tested in LOX/GH2. The result of the testing was that post inspection showed that the nozzles remained in good condition and leak-free. The success of this experimentation supports the concept that 3D printing can be applied to larger-scale rocket engines for use in government and industrial programs.

1.2.2   Surface roughness

When considering the manufacturing of products, roughness is an important parameter to consider due to its effect on the flow around an object. Depending on the type of manufacturing, whether it be traditional or additive, there is a degree of roughness to the surface that will, in turn, affect the boundary layer transition from laminar to turbulent flow. Taking a look at Figure 1.10, roughness heights are shown in regard to what the manufacturing process was used.

PROCESS	50 (2000)	25 (1000)	12.5 (500)	6.3 (250)	3.2 (125)	1.6 (63)	0.80 (32)	0.40 (16)	0.20 (8)	0.10 (4)	0.05 (2)	0.025 (1)	0.012 (0.5)	μ m (μ in)
Flame Cutting														
Sawing														
Planing, Shaping														
Drilling														
Elec. Discharge Mach.														
Milling														
Broaching														
Reaming														
Laser														
Boring, Turning														
Roller Burnishing														
Grinding														
Honing														
Polishing														
Lapping														
Superfinishing														

KEY:
Less Frequent Application =
Average Application =

The ranges shown above are typical of the process listed. Higher or lower values may be obtained under special conditions.

Figure 1.10 - Manufacturing process roughness [9]

In "*Experimental Investigation of Roughness Effects on Transition on Blunt Spherical Capsule Shapes*", Rolf Radespiel and associates discuss how surface roughness affects the boundary layer transition of blunt objects in hypersonic flow. This is important to the design of blunt nose cones as it affects the flow characteristics such as the Reynolds number(Re), enthalpy, and wall temperatures as they vary during flight. From the study, it was found that when inducing roughness heights, there was a correlation to the thickness of the boundary layer. When the freestream was introduced to the rough patches, depending on the degree of roughness or the roughness height, there would be a quicker transition from laminar to turbulent flow. This helped to confirm how surface roughness for vehicle design aided in transient growth.

1.2.3   Blunt nose cone angle

The nose cone of a vehicle is meant to travel through compressible fluid, thus it must experience minimal resistance when traveling. For smoother flow over the surface, nose cones are blunted rather than with a pointed edge. Depending on the type of mission, the nose cone angle would vary, changing the size and shape of the nose cone. "*CFD Analysis of Various Nose Profiles*" by A Sanjay Varma et. al details the various aerodynamics profiles of some nose cones. Run through ANSYS at Mach 0.8, performance characteristics are displayed. Table 1.1 shows the various nose profiles used for the study as well as the equations to create the shape.

Table 1.1 - Nose cone profiles [11]

S. No	Nose Profile	Equations	Shape
1	Cone	$y = \dfrac{xR}{L}$	
2	Parabola	$y = R\left(\dfrac{x}{L}\right)^{n}$ n=0.5	
3	Ogive	$\rho = \dfrac{R^2 + L^2}{2R}$	
4	Von Karman Ogive	$\theta = cos^{-1}\left[1 - \dfrac{2x}{L}\right]$ $y = \dfrac{R\sqrt{\theta - \dfrac{sin(2\theta)}{2} + C sin^3}}{\sqrt{\pi}}$ C=0	

After the profiles were run through ANSYS, a pressure and mach comparison were presented where it can be seen how the cone angle affects the different profiles in regard to the two parameters. Looking at Figure 1.11, it can be seen how the sharp point cone has a longer length profile of pressure thus resulting in a higher absolute pressure at a lower Mach value for the CFD. As for the blunted cones, the pressure was greater at the tip but severely lowered along the length of the nose while the Mach values tended to be on the higher side.
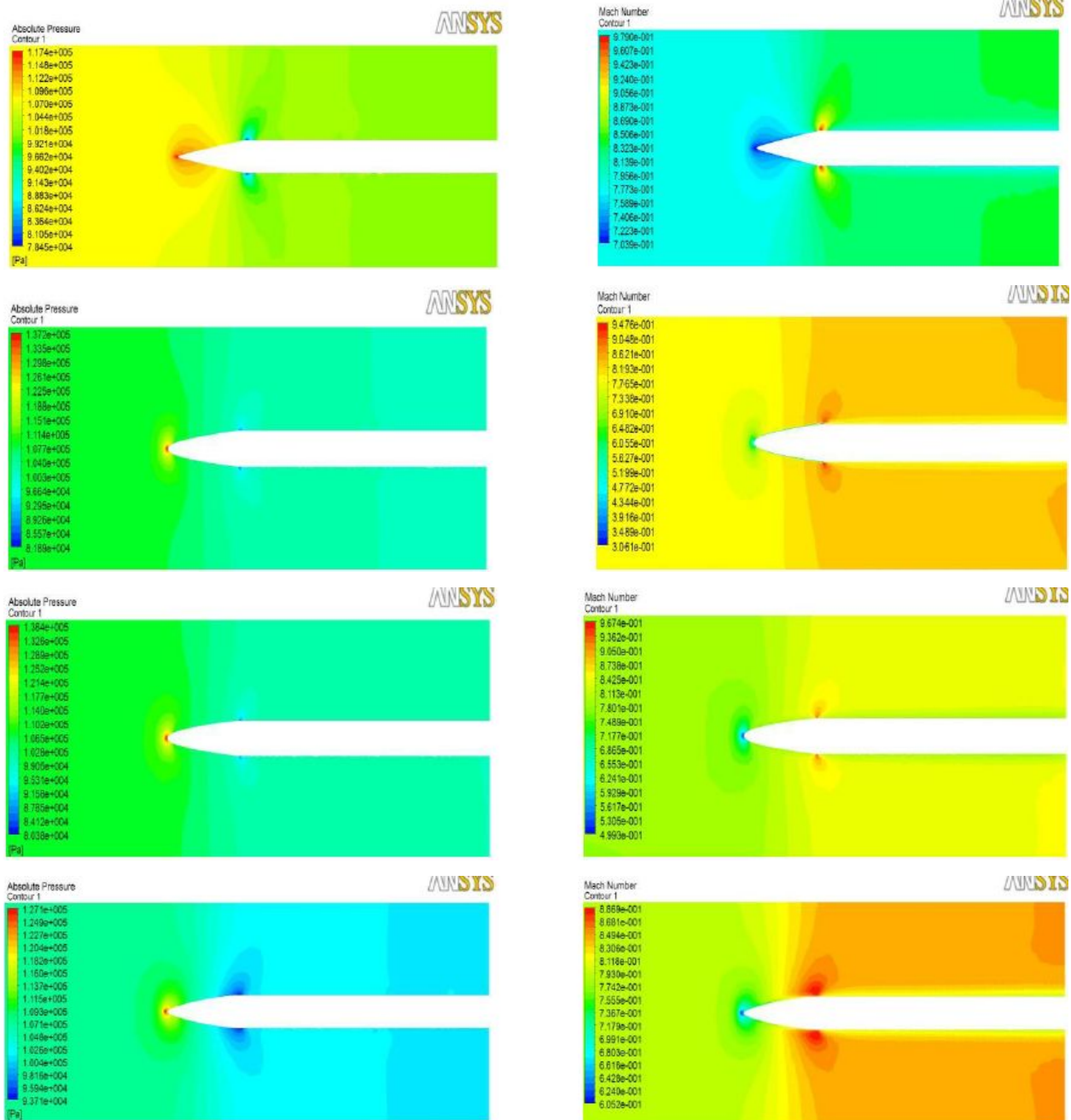
Figure 1.11 - Pressure and Mach contours of conical, ogive, parabola, and von Karman
(Top to Bottom) [11]

1.2.4   Boundary layer transition

Boundary layer transition is the point on the surface when freestream flows transition from laminar to turbulent flow. The characterization of flow is determined by Reynold's number. If Re is below 2100, then it is laminar and if it is above 4000, then its turbulent[12]. The range is where the transition would occur depending on the surface roughness when the flow starts around the object. The Reynolds number correlates to the thickness of the boundary layer. Re is the ratio of inertial to viscous forces in a fluid, thus as turbulence increases, so does Re and by extension, the boundary layer thickness. Equation 1.1

$$Re = \frac{\rho V D}{\mu}$$
(1.1)

An important theory for this project would be the boundary layer theory in which higher Re equals less viscosity, as it develops an understanding of how the transition point moves when introducing a viscous source (surface roughness) to the nose cones. The transition point change would signify the change in boundary layer thickness as well as the change from laminar heating to turbulent heating.

In a study titled "*Transition Experiments on Large Bluntness Cones with Distributed Roughness in Hypersonic Flight*", Daniel C. Reda and company performed an experiment in which large blunt cones were flown at Mach 10 to analyze boundary layer transition over a roughened surface. From the experiment, it was found that Re was at its maximum at the start of the rough surface and decreased along the length of the surface. The induced transition occurred downstream of the maximum location, but then upstream to the start point as pressure was increased. In Figure 1.12, it can be seen that when pressure increases, the transition begins to move upstream.
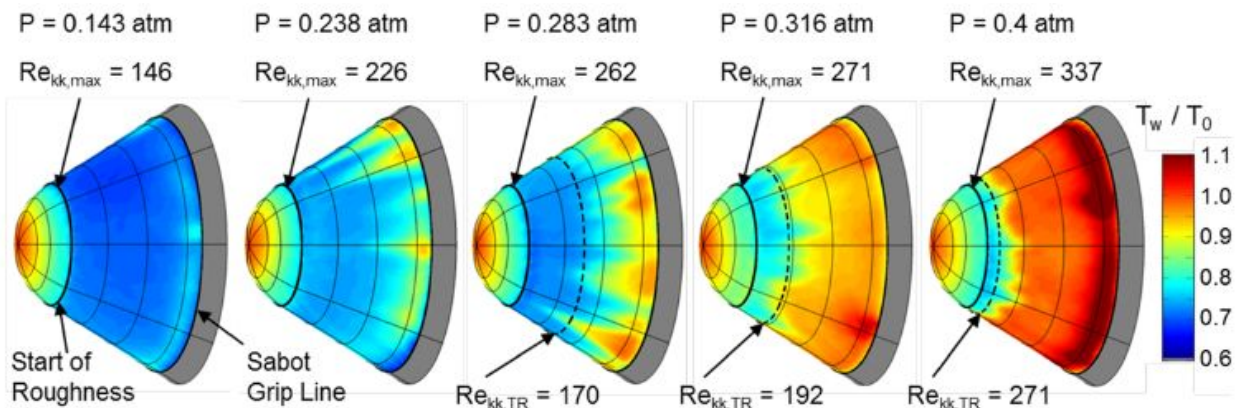
Figure 1.12 - Measured transition change along with pressure increase [13]

1.2.5 Shock wave - oblique v expansion

Shock waves are resultant of a flow's change in static properties due to collisions of multiple freestreams. The various types are normal, oblique, expansion, attached, and detached shock waves. For this project in particular, the shocks found are attached, oblique, and expansion.

An attached shock is where the shock wave remains intact with the leading edge of an object while in a supersonic flow field. Considering the conditions for the project's CFD, it can be assumed that the shock will not detach due to the low speed in relation to the nose cone's angle of attack.
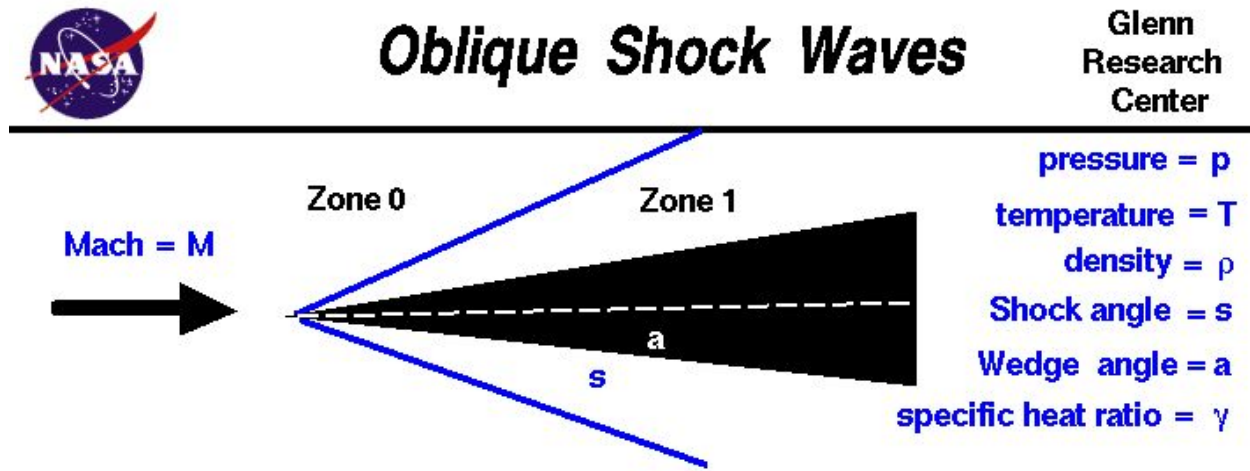
Figure 1.13 - Oblique shock wave diagram (NASA) [14]

$$\frac{p_2}{p_1} = 1 + \frac{2\gamma}{\gamma + 1}(M_1^2 \sin^2 \beta - 1) \qquad (1.2)$$

$$\frac{\rho_2}{\rho_1} = \frac{(\gamma + 1)M_1^2 \sin^2 \beta}{(\gamma - 1)M_1^2 \sin^2 \beta + 2} \qquad (1.3)$$

$$\frac{T_2}{T_1} = \frac{p_2}{p_1} \frac{\rho_1}{\rho_2}. \qquad (1.4)$$

$$M_2 = \frac{1}{\sin(\beta - \theta)} \sqrt{\frac{1 + \frac{\gamma - 1}{2}M_1^2 \sin^2 \beta}{\gamma M_1^2 \sin^2 \beta - \frac{\gamma - 1}{2}}}. \qquad (1.5)$$

Oblique shocks occur when a normal shock deflects off the surface of an object, restricting its flow. Across this shock, pressure, temperature, gas density, and entropy also increase as mach

decreases. However, enthalpy and total temperature stay constant. Referencing Figure 1.13, the oblique shock is shown as an inclined line separating from the nose cone. Equations 1.2- 1.5 [14] can be used to calculate the change in static properties across the wave for an oblique shock. For the project, the oblique shocks will appear at the leading edge of the nose cone as shown in Figure 1.13, from there the stream will transition to expansion waves as it leaves the trailing edge of the nose cone.
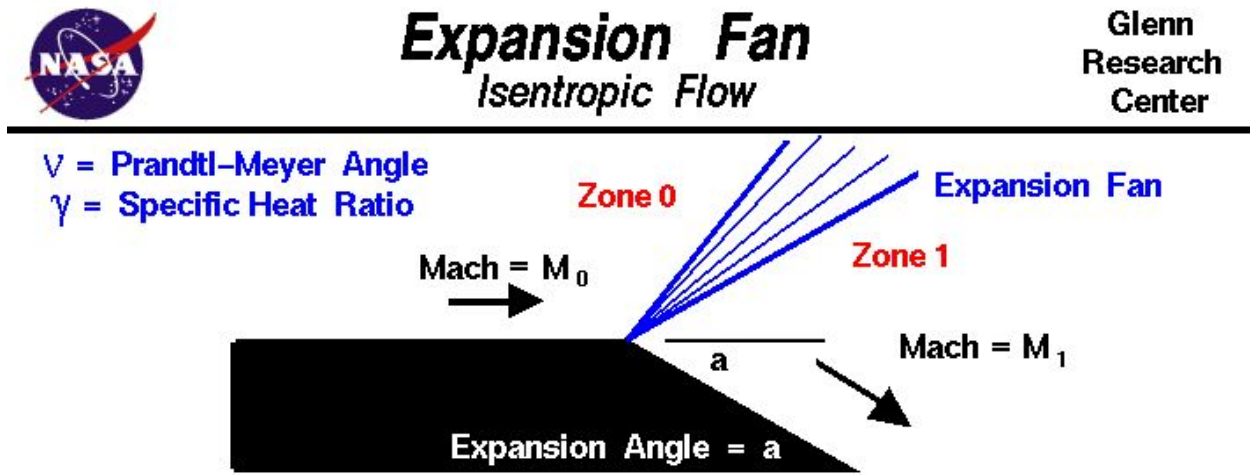
Figure 1.14 - Expansion shock wave diagram (NASA) [15]

$$\frac{T_2}{T_1} = \left(\frac{1 + \frac{\gamma-1}{2}M_1^2}{1 + \frac{\gamma-1}{2}M_2^2}\right) \tag{1.6}$$

$$\frac{p_2}{p_1} = \left(\frac{1 + \frac{\gamma-1}{2}M_1^2}{1 + \frac{\gamma-1}{2}M_2^2}\right)^{\frac{\gamma}{\gamma-1}} \tag{1.7}$$

$$\frac{\rho_2}{\rho_1} = \left(\frac{1 + \frac{\gamma-1}{2}M_1^2}{1 + \frac{\gamma-1}{2}M_2^2}\right)^{\frac{1}{\gamma-1}}. \tag{1.8}$$

$$\theta = \nu(M_2) - \nu(M_1) \tag{1.9}$$

$$\nu(M) = \int \frac{\sqrt{M^2 - 1}}{1 + \frac{\gamma-1}{2}M^2}\frac{dM}{M} \tag{1.10}$$

$$= \sqrt{\frac{\gamma+1}{\gamma-1}}\arctan\sqrt{\frac{\gamma-1}{\gamma+1}(M^2-1)} - \arctan\sqrt{M^2-1}. \tag{1.11}$$

The opposite of an oblique shock wave, an expansion wave means an increase of the flow area. Unlike oblique shock waves, expansion waves have increased mach, decreased pressure, and are also isentropic [15]. Calculation of the properties across the shock requires the use of the Prandtl-Meyer function which is the angle by which mach is increased [15]. To calculate the mach by means of the Prandtl-Meyer, equations 1.9 - 1.11 [15] can be used. Finding the mach before and after the shock allows the use of equations 1.6 - 1.8 [15] to calculate static property changed. Looking at Figure 1.14, the blue inclined lines represent the expansion waves as the expansion angle gives way to a flow area increase. Taking that angle, the mach after the shock and its coordinating properties can be calculated. For the nose cone, the expansion wave would occur on the trailing edge.

1.2.6   Turbulent heating

When an object has a laminar flow on the surface, the heat transfer tends to be low due to the lack of chaos and thus pressure causing the exchange of heat[16]. For turbulent flow, the opposite will happen. Thus, when considering the roughness of a blunt cone, the change in the level of heat transfer from when the flow transitions is important as it affects what type of mission the nose cone can be used for.

In 2017, Brian R. Hollis conducted an "*Experimental Investigation of Roughness Effects on Transition Onset and Turbulent Heating Augmentation on a Hemisphere at Mach 6 and Mach 10*". The investigation studied how surface roughness affected boundary-layer transition and turbulent heating. Using models with roughness to represent heat shield ablation, they were run through hypersonic wind tunnel testing at Mach 6 and 10. The results were then compared to Computational Fluid Dynamics (CFD) simulations with smooth surfaces. The results of the study were that when roughness heights were increased, the transition point would move upstream, increasing turbulent heat levels.

1.3   Project proposal

The objective of this project is to study the change in transition point from laminar to turbulent flow of various angled blunt nose cones at different degrees of surface roughness and to derive a relationship between surface roughness and turbulent heating.

1.4   Methodology

This project will use Reda's *Transition Experiments on Large Bluntness Cones with Distributed Roughness in Hypersonic Flight*, performed at the Hypervelocity Free Flight Aerodynamic Facility at NASA Ames, as the basis for running simulations through ANSYS. Using the geometry provided in the journal, a simulation will be done with the same conditions to see the results are similar to one another. From there, the geometry's nose angle and the surface roughness will be altered to see how these changes affect the flow's transition point. Figure 1.15 shows the base design and measurements for the preliminary 3D geometry of the CFD.

θ_c = 30 degrees
R_N = 0.3 in (7.62 mm), smooth
D_B = 1.191 in (30.25 mm)
L = 0.739 in (18.77 mm)

Figure 1.15 - Base geometry parameters from Reda [15]

After taking this design and simulating it, θ_c which is cone angle and R_N which is roughness height will be altered and simulated. The proposed cases are in Table 1.2.

Table 1.2 - Parametric cases for CFD

Angle(Degrees) θ_c	Surface Roughness Height(μm)
30	0
	3
	5.60
	10
45	0
	3
	5.60
	10
60	0
	3
	5.60
	10

Since the paper is based on a real-life experiment, some parameters will be assumed when running through CFD. A fine mesh will be used, with possible real-life physics being applied such as real gas, viscosity, thermal, etc. After running all cases, the simulations will be compared to prove a correlation between surface roughness and turbulent heating.

As stated earlier, the project will be accomplished through the means of ANSYS (CFD Software), entailing the use of computational models and grid generation to solve for the desired characteristics for comparison to find the correlation. The program will use Navier-Stokes equations of momentum and continuity to simulate the motion of fluid to portray fluid behavior over the surface of the several nose cones. Equation 1.11 displays the conservation of momentum in cartesian coordinates. This equation is derived into equations 1.12-1.14 where it displays the momentum equation into its three-dimensional components [19].

$$\rho \frac{DV}{Dt} = -\nabla P + \mu \nabla^2 V + \rho g \qquad (1.11)$$

$$\rho\left(\frac{\partial V_x}{\partial t}+V_x\frac{\partial V_x}{\partial x}+V_y\frac{\partial V_x}{\partial y}+V_z\frac{\partial V_x}{\partial z}\right)=-\frac{\partial P}{\partial x}+\mu\left[\frac{\partial^2 V_x}{\partial x^2}+\frac{\partial^2 V_x}{\partial y^2}+\frac{\partial^2 V_x}{\partial z^2}\right]+\rho\,g_x \qquad (1.12)$$

$$\rho\left(\frac{\partial V_y}{\partial t}+V_x\frac{\partial V_y}{\partial x}+V_y\frac{\partial V_y}{\partial y}+V_z\frac{\partial V_y}{\partial z}\right)=-\frac{\partial P}{\partial y}+\mu\left[\frac{\partial^2 V_y}{\partial x^2}+\frac{\partial^2 V_y}{\partial y^2}+\frac{\partial^2 V_y}{\partial z^2}\right]+\rho\,g_y \qquad (1.13)$$

$$\rho\left(\frac{\partial V_z}{\partial t}+V_x\frac{\partial V_z}{\partial x}+V_y\frac{\partial V_z}{\partial y}+V_z\frac{\partial V_z}{\partial z}\right)=-\frac{\partial P}{\partial z}+\mu\left[\frac{\partial^2 V_z}{\partial x^2}+\frac{\partial^2 V_z}{\partial y^2}+\frac{\partial^2 V_z}{\partial z^2}\right]+\rho\,g_z \qquad (1.14)$$

Equation 1.15 shows the continuity equation which when simplified equals the the conversation of mass (equation 1.16) along the surface of a model.

$$\frac{\partial \rho}{\partial t}+\frac{\partial}{\partial x}\left(\rho V_x\right)+\frac{\partial}{\partial y}\left(\rho V_y\right)+\frac{\partial}{\partial z}\left(\rho V_z\right)=0 \qquad (1.15)$$

$$\frac{\partial \rho}{\partial t}+\nabla.\left(\rho V\right)=0 \qquad (1.16)$$

To account for the conservation of energy as the flow travels against the surface, the energy equation (equation 1.17) is used. This will help to understand that as the flow turns from laminar to turbulent, the energy is being conserved [20].

$$\begin{aligned}
\frac{\partial(e+V^2/2)}{\partial t}=&-u\frac{\partial(e+V^2/2)}{\partial x}-v\frac{\partial(e+V^2/2)}{\partial y}\\
&+\frac{1}{\rho}\left\{\frac{\partial}{\partial x}\left(k\frac{\partial T}{\partial x}\right)+\frac{\partial}{\partial y}\left(k\frac{\partial T}{\partial y}\right)-\frac{\partial(pu)}{\partial x}-\frac{\partial(pv)}{\partial y}\right.\\
&\left.+\frac{\partial(u\tau_{xx})}{\partial x}+\frac{\partial(u\tau_{yx})}{\partial y}+\frac{\partial(v\tau_{xy})}{\partial x}+\frac{\partial(v\tau_{yy})}{\partial y}\right\}
\end{aligned} \qquad (1.17)$$

The turbulent viscosity is a factor to consider when regarding the change of static temperature and transient point. For the simulation, k-epsilon viscosity was used, presented in equations 1.18 and 1.19, where k is turbulent kinetic energy, and epsilon is turbulent dissipation [21].

$$\frac{\partial(\rho k)}{\partial t}+\frac{\partial(\rho k u_i)}{\partial x_i}=\frac{\partial}{\partial x_j}\left[\frac{\mu_t}{\sigma_k}\frac{\partial k}{\partial x_j}\right]+2\mu_t E_{ij}E_{ij}-\rho\varepsilon \qquad (1.18)$$

$$\frac{\partial(\rho\varepsilon)}{\partial t}+\frac{\partial(\rho\varepsilon u_i)}{\partial x_i}=\frac{\partial}{\partial x_j}\left[\frac{\mu_t}{\sigma_\varepsilon}\frac{\partial\varepsilon}{\partial x_j}\right]+C_{1\varepsilon}\frac{\varepsilon}{k}2\mu_t E_{ij}E_{ij}-C_{2\varepsilon}\rho\frac{\varepsilon^2}{k} \qquad (1.19)$$

Considering the method of investigation and the theories behind it, the project will give further insight into how nose cones affect the performance of vehicles, and thus can be applied to future designs and missions.

2.   Experimental tools and methods

2.1   Blunt cone designs

For this experiment, the designs for the blunt nose cones are based on the parameters shown in Figure 2.1. Taking these dimensions into account, they were input into Autodesk inventor to be drawn.
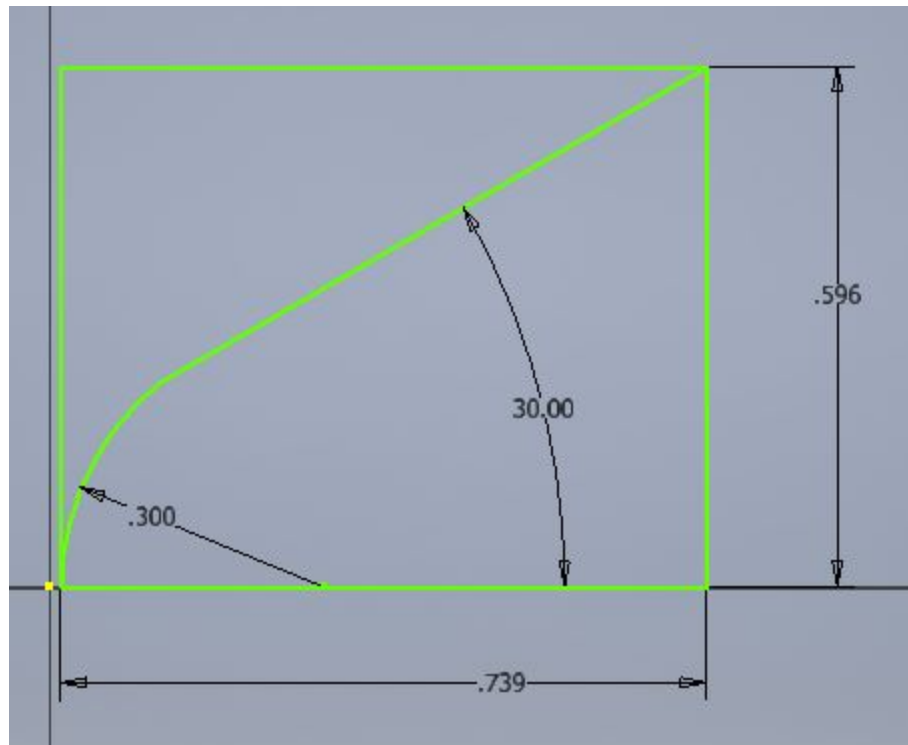
Figure 2.1 - Reda design drawn in Autodesk Inventor
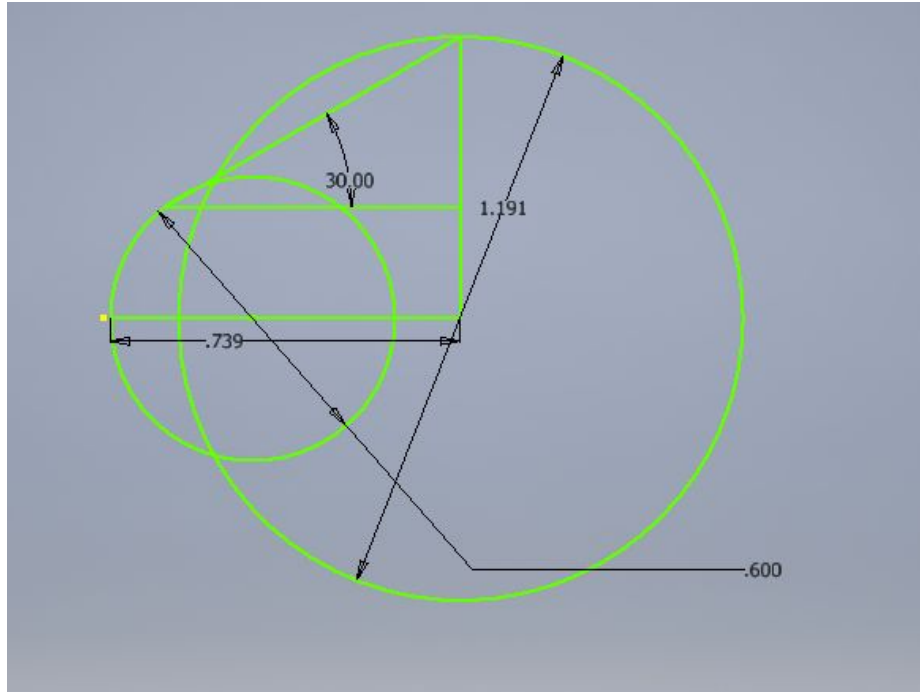
Figure 2.2 - Design method for the base blunt nose cone

The spherically blunted nose cone that Reda used is recreated in CAD by having a triangle meet a circle tip. Looking at Figure 2.2, it can be seen how the two shapes intersect and have a point of tangency. Trimming the unnecessary lines, the design in Figure 2.1 was created.

In the article this design was drawn from, Reda didn't give any equations for the nose cone design, nor any reason why it was the design picked for the experiment. However, it is possible to explain the concept behind designing a nose cone's shape.
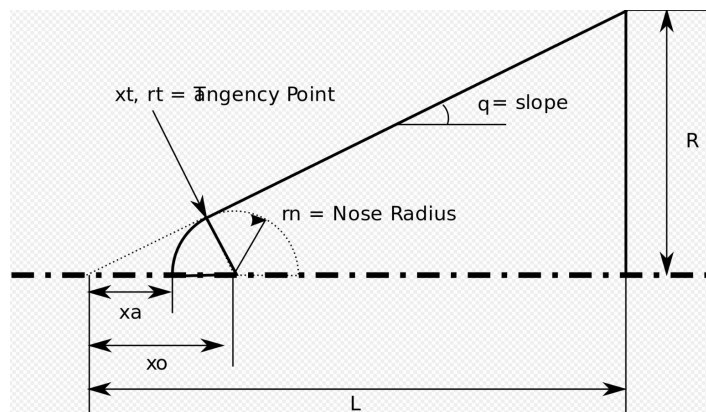
Figure 2.3 - Blunt nose cone geometry [21]

Looking at Figure 2.3, it can be seen how the nose cone starts as a triangle but rounds out after hitting a tangential point with a circle, which is exactly what happened in Figure 14 for Reda's design recreation [20].

$$x_t = \frac{L^2}{R}\sqrt{\frac{r_n^2}{R^2 + L^2}} \qquad (2.1)$$

$$y_t = \frac{x_t R}{L} \qquad (2.2)$$

Using the above equations, it is possible to calculate the location of the tangency point coordinate (x,y) where the circle meets the triangle, thus allowing a smooth transition between the two shapes [22].

$$x_o = x_t + \sqrt{r_n^2 - y_t^2} \qquad (2.3)$$

$$x_a = x_o - r_n \qquad (2.4)$$

In the case of not using 3D modeling software, the above two equations would be used to solve for xa and xo (refer to Figure 2.3). These two variables can be used in turn to solve other geometry dimensions such as the length (L) and radius of the sphere (rn) being applied to the cone geometry.

Besides the base nose cone design, there are 2 more designs for experimentation. The constant variable for all the designs is the length of the nose cone and the nose cone radius. The parameter being adjusted is the angle of the nose cone, in turn, changing the length of the bottom of the nose cone (variable R). This is apparent in Figures 16 & 17.
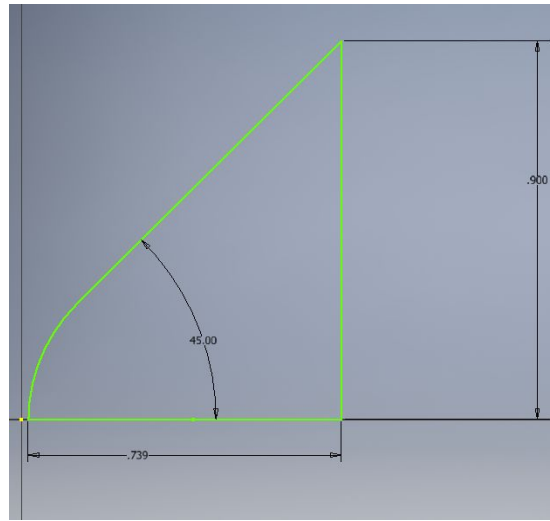
Figure 2.4 - Blunt nose cone at angle 45 degrees
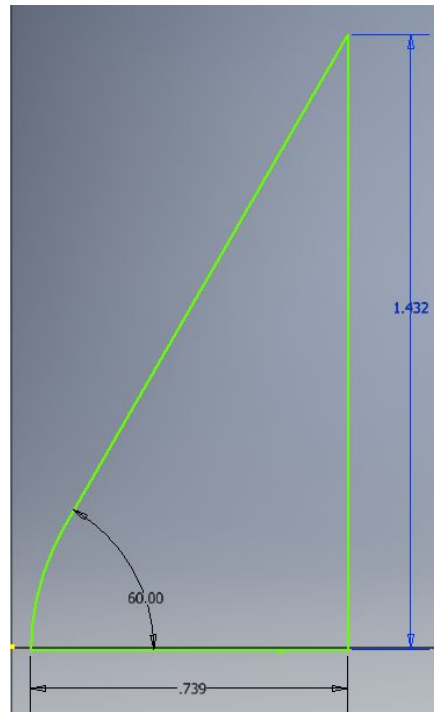
Figure 2.5 - Blunt nose cone at an angle 60 degrees

It can be seen that as the angle increased in size, so did the length of the bottom of the nose cone. This change is a result of the desired dimensions as well as the constraints placed on the geometrical geometry as tangency perpendicularity. The completed 2D geometries were then turned into 3D models.

2.2   3D Models

With the 3 designs already input into Autodesk Inventor, the next step is turning them into 3D models that can be run as 3D simulations through ANSYS. By simply revolving around the x-axis, we get the models below in Figures 18-20.
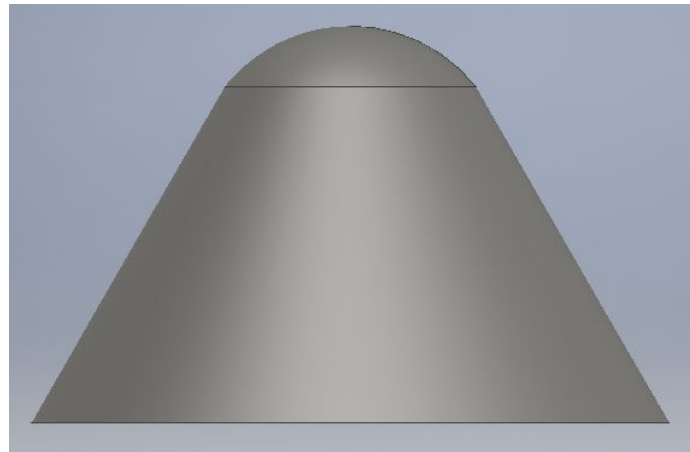
Figure 2.6 - 3D blunt nose cone at 30 degree angle
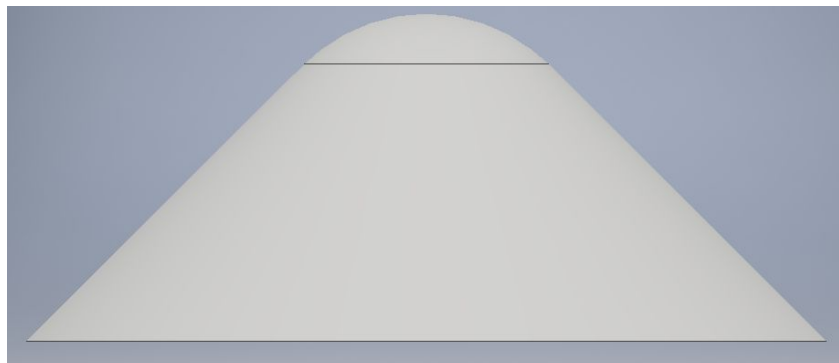
Figure 2.7 - 3D blunt nose cone at 45 degree angle
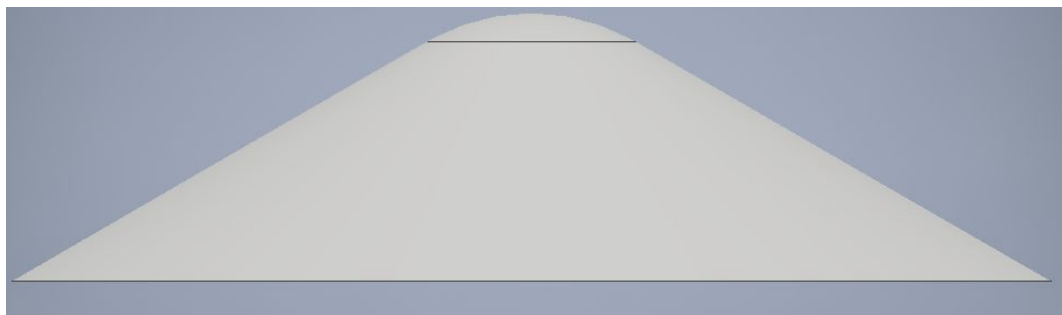
Figure 2.8 - 3D blunt nose cone at 60 degree angle

2.3   Simulations

2.3.1   Enclosure

Reda's experiment was designed to analyze how surface roughness would affect the flow over a blunt nose cone. For his design, he had the tip of the nose smooth while the side had a roughness height of 5.6 μm. As for the actual experimentation, Reda manufactured his design and ran it through a wind tunnel at Mach 10.

For this experiment, the design differs in regards to the fact that the entire cone will have a uniformly rough surface. Due to limited resources, the present experiment was conducted by means of CFD simulations through ANSYS.

Taking the 3D models from Inventor, they were input into ANSYS. Since this project focuses on analyzing the flow around the blunt cones, the models were placed into enclosures. Then a boolean was set up to subtract the volume of the nose cones away from the fluid domain area. The final step before meshing was naming the sides: inlet, outlet, walls, and fluid domain. Figures 21-23 show these first few steps.

Figure 2.9 - Enclosed 30 degree blunt nose cone
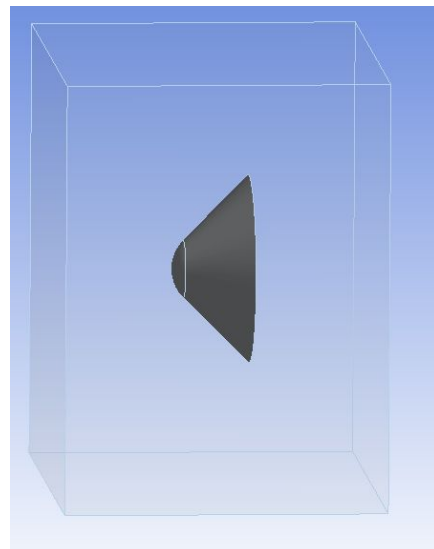
Figure 2.10 - Enclosed 45 degree blunt nose cone
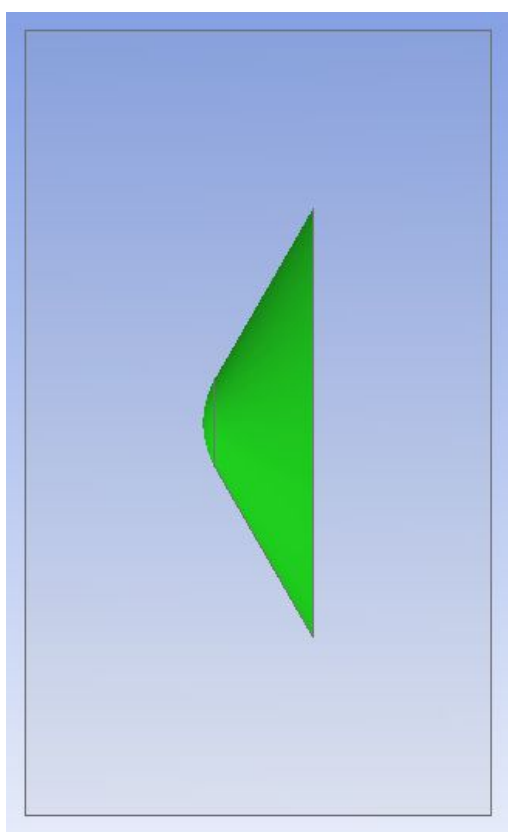
Figure 2.11 - Enclosed 60 degree blunt nose cone

2.3.2 Mesh

In Figures 2.13-2.15, the meshes are presented. Since Reda's experiment was run through a wind tunnel, there were no direct parameters set for mesh sizing and quality. To simplify the method of simulation, most features of the mesh were left as "program controlled". The element order was linear with an element size of .0008m. The assembly meshing method is tetrahedron and finely meshed with a smooth transition. A basic overview of the mesh settings as seen in Figure 2.12, numbers may slightly vary with the model.

Details of "Mesh"	
Display	
Display Style	Use Geometry Setting
Defaults	
Physics Preference	CFD
Solver Preference	Fluent
Element Order	Linear
Element Size	8.e-004 m
Export Format	Standard
Export Preview Surface Mesh	No
Sizing	
Use Adaptive Sizing	No
Growth Rate	Default (1.2)
Max Size	Default (1.6e-003 m)
Mesh Defeaturing	Yes
Defeature Size	Default (4.e-006 m)
Capture Curvature	Yes
Curvature Min Size	Default (8.e-006 m)
Curvature Normal Angle	Default (18.0°)
Capture Proximity	No
Bounding Box Diagonal	0.20358 m
Average Surface Area	9.5519e-003 m²
Minimum Edge Length	3.3574e-002 m
Quality	
Check Mesh Quality	Yes, Errors
Target Skewness	Default (0.900000)
Smoothing	High
Mesh Metric	None
Inflation	
Use Automatic Inflation	None
Inflation Option	Smooth Transition
Transition Ratio	0.272
Maximum Layers	5
Growth Rate	1.2
Inflation Algorithm	Pre
View Advanced Options	No
Assembly Meshing	
Method	None
Advanced	
Number of CPUs for Parallel...	Program Controlled
Straight Sided Elements	
Rigid Body Behavior	Dimensionally Reduced
Triangle Surface Mesher	Program Controlled
Topology Checking	Yes
Pinch Tolerance	Default (7.2e-006 m)
Generate Pinch on Refresh	No
Statistics	
Nodes	895056
Elements	4921314

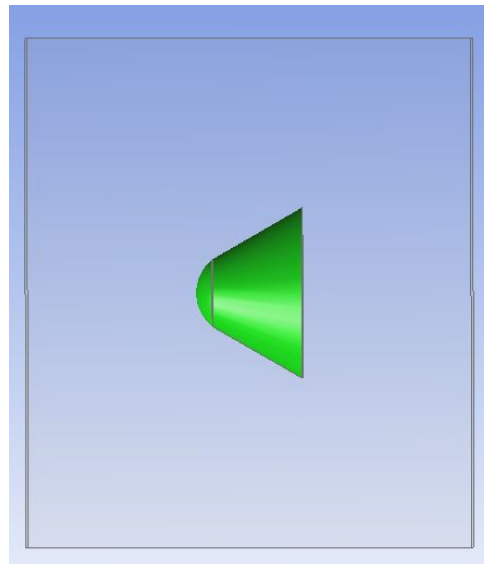Figure 2.12 - Mesh details overview for 30 degrees blunt nose cone
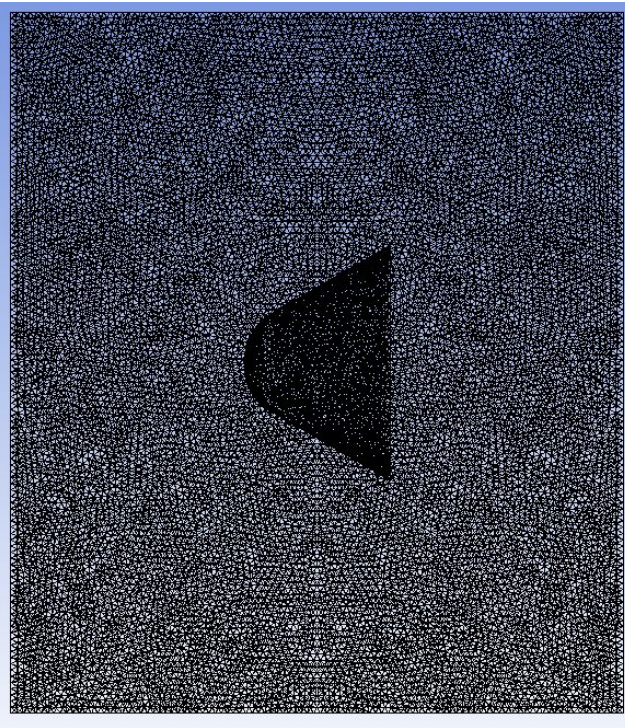
Figure 2.13 - Meshed 30 degree blunt nose cone
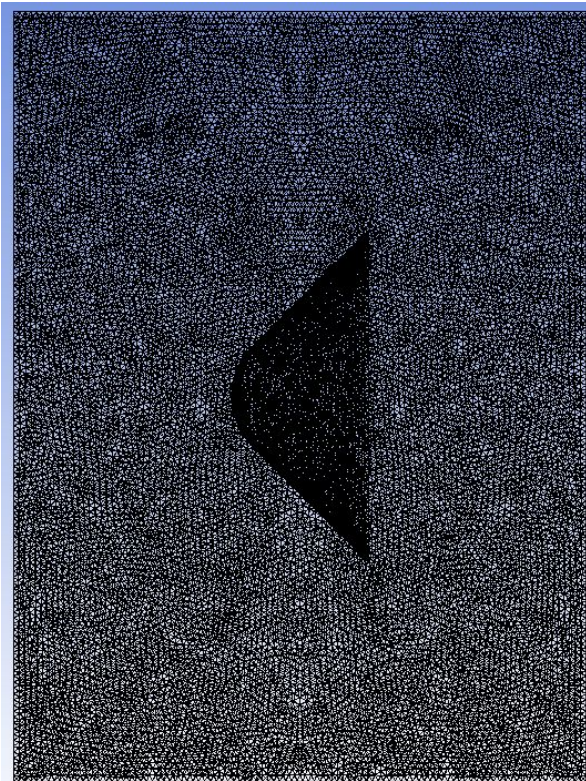
Figure 2.14 - Meshed 45 degree blunt nose cone
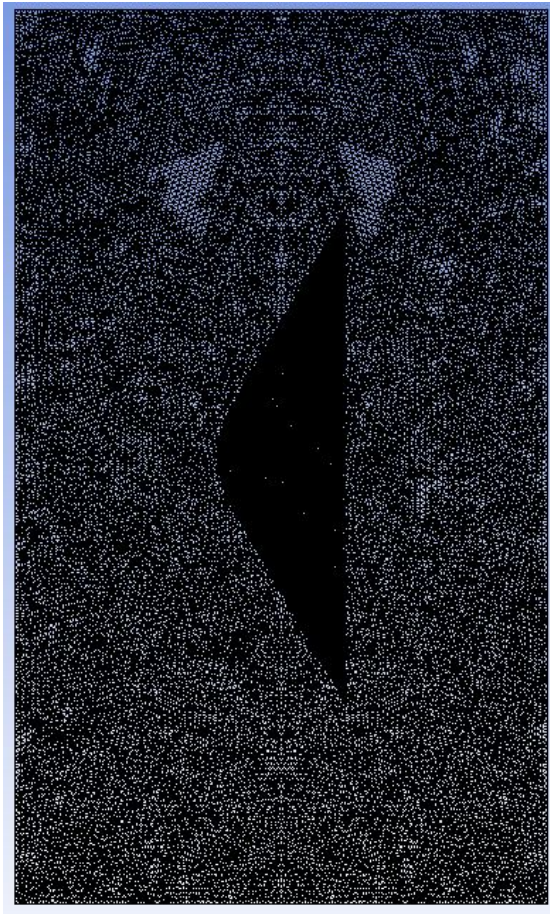
Figure 2.15 - Meshed 60 degree blunt nose cone

2.3.3   Setup

Prior to simulations, physical conditions have to be set up to get the desired results from the 3D model. Since Reda had performed his experiment in real life, the CFD for this experiment must represent this to have a good comparison of the experimental nose cones to Reda's.

ANSYS Fluent was launched with double precision and serial processing. The solver was set to pressure-based with relative velocity and transient time. Gravity was considered at an acceleration of 9.8 m/s^2. Viscous force is set as a realizable k-epsilon model with viscous heating. To determine the change of temperature along the surface, the energy equation was invoked. The materials used are air for fluid and steel for solid. To set up the conditions of a wind tunnel, the inlet was set as velocity based with a speed of Mach 10, and the outlet was put as pressure based. The solution method used was a second-order spatial discretization. For the solution initialization, it was standard with initial values of pressure as 101325 pascals and velocity as Mach 10 while turbulent values were presumed by the program. The wall roughness was set at 0, 3, 5.6, and 10 µm for each model. Finally, the simulation was set at a time step of

20 with a max iteration of 10. In Appendix A, a detailed example is given for the solver conditions of the 30 degree nose cone at 0 μm roughness prior to timestep and iterations. The rest of the cases were similar to this, with the exception of zone naming being different.

3. Results

3.1 Reda results
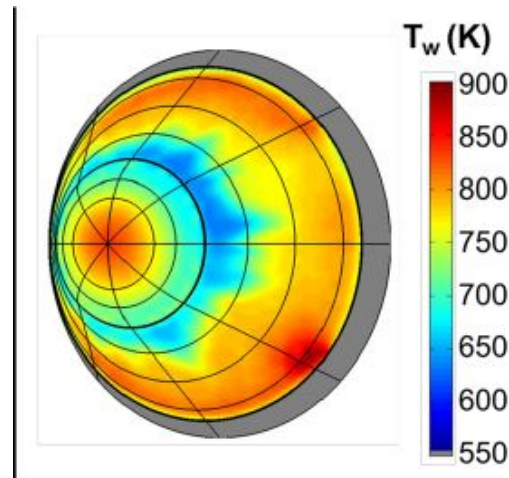
Figure 2.16 -Reda cone wall temperature 30 degree angle @ 5.6 µm [13]

3.2 ANSYS results

3.2.1 Cone angle 30 degrees
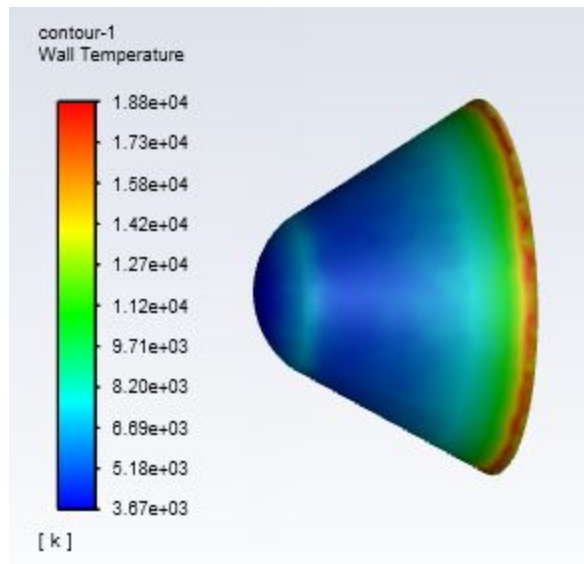
Figure 2.17 - Contour of 30 degree nose cone w/ surface roughness of 0 µm
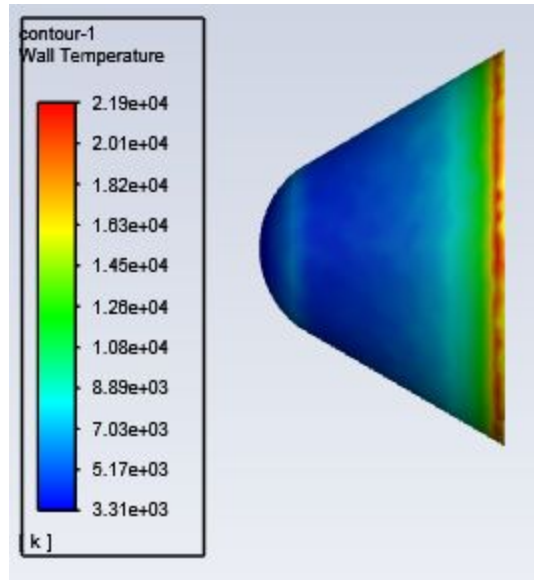
Figure 2.18 - Contour of 30 degree nose cone w/ surface roughness of 3 µm
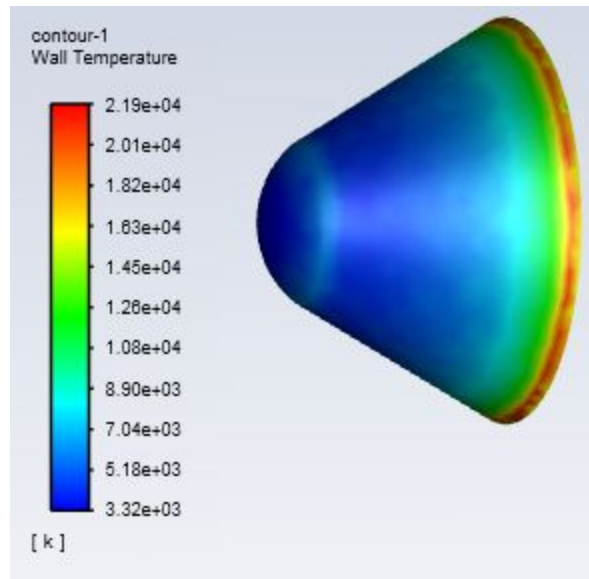
Figure 2.19 - Contour of 30 degree nose cone w/ surface roughness of 5.6 µm
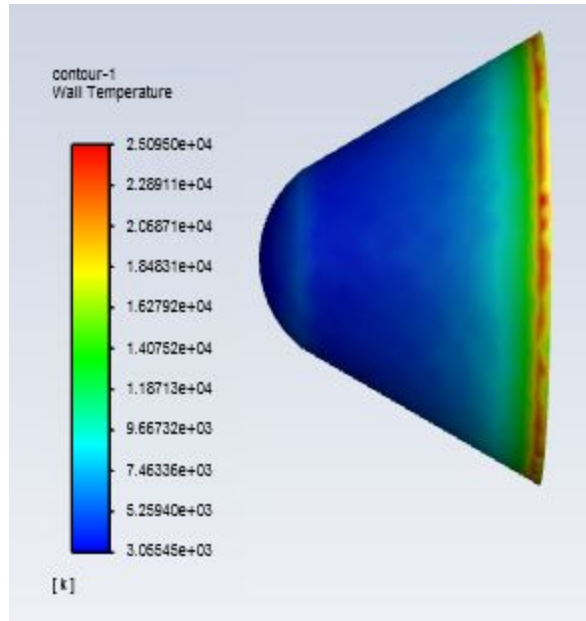
Figure 2.20 - Contour of 30 degree nose cone w/ surface roughness of 10 µm

3.2.2 Cone angle 45 degrees
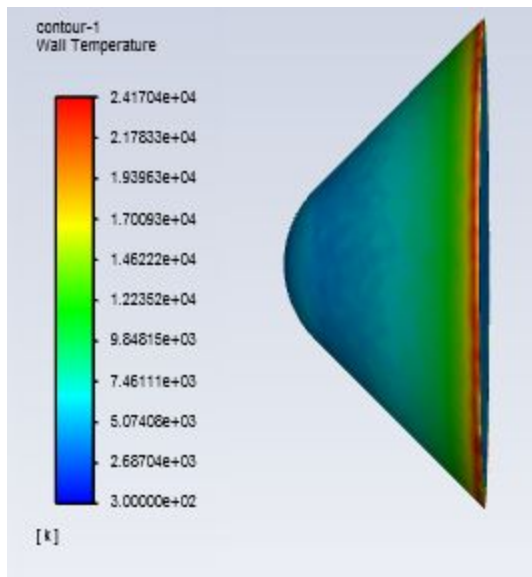
Figure 2.21 - Contour 45 degree nose cone w/ surface roughness of 0 µm
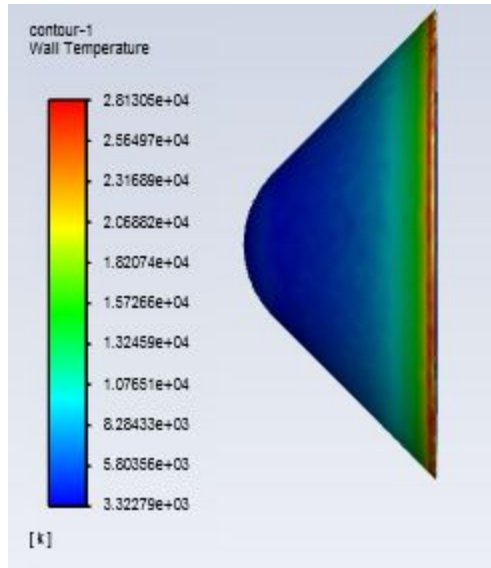
Figure 2.22 - Contour of 45 degree nose cone w/ surface roughness of 3 µm
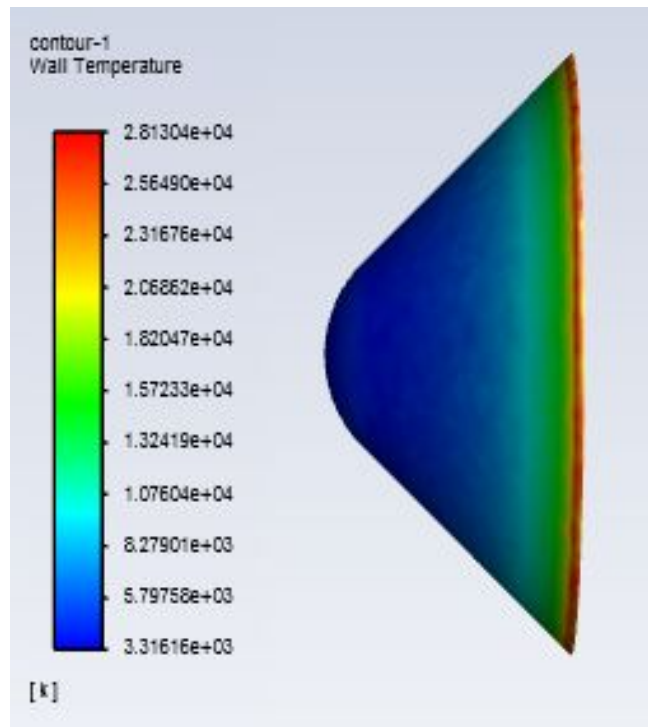
Figure 2.23 - Contour of 45 degree nose cone w/ surface roughness of 5.6 µm
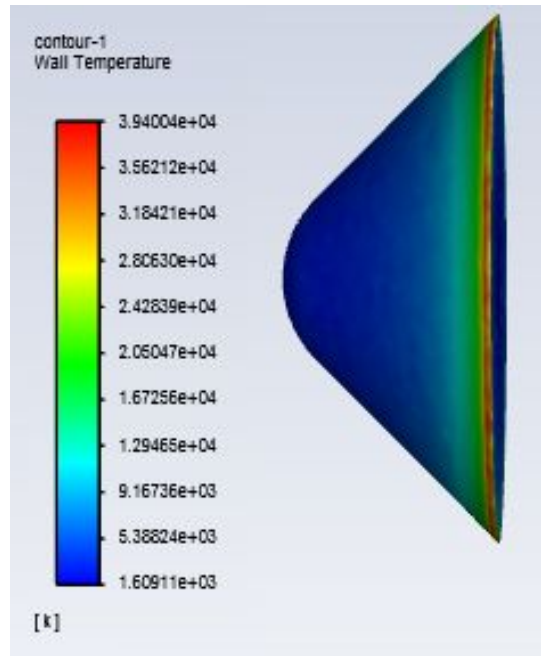
Figure 2.24 - Contour of 45 degree nose cone w/ surface roughness of 10 μm

3.2.3   Cone angle 60 degrees
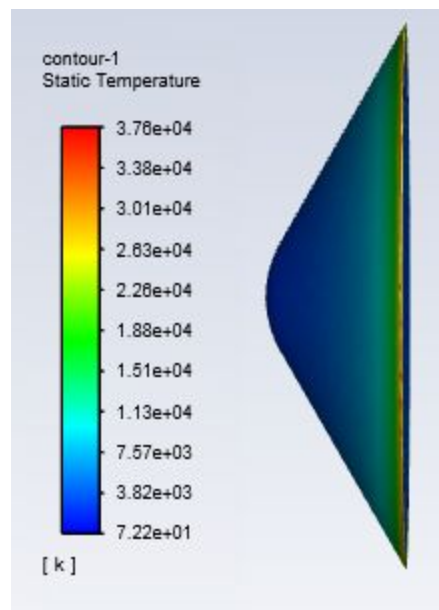
Figure 2.25 - Contour of 60 degree nose cone w/ surface roughness of 0 μm
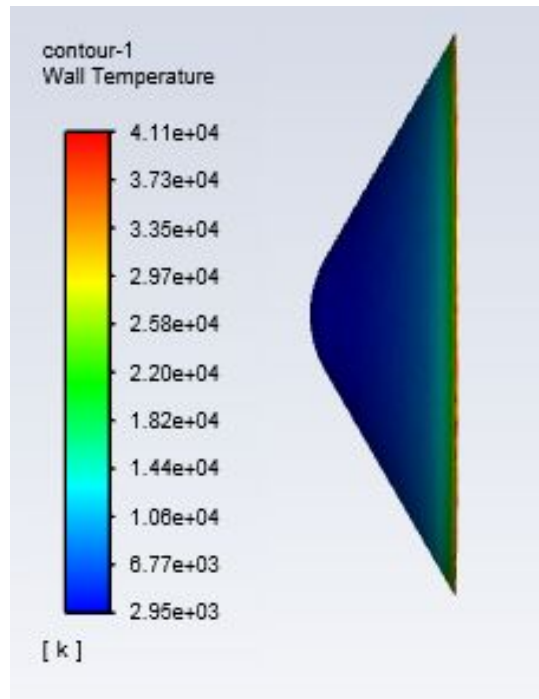
Figure 2.26 - Contour of 60 degree nose cone w/ surface roughness of 3 µm
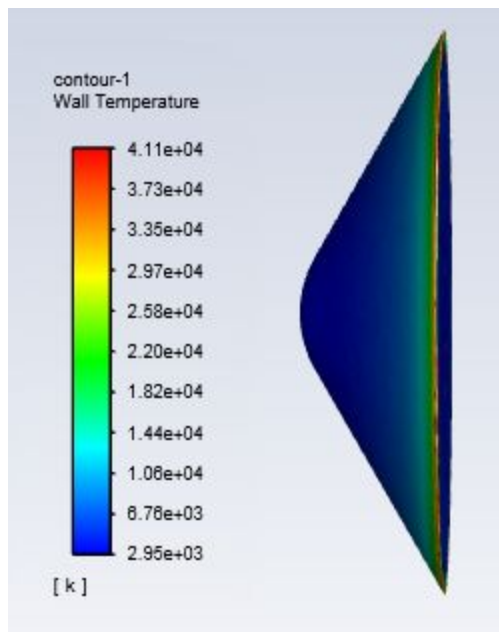
Figure 2.27 - Contour of 60 degree nose cone w/ surface roughness of 5.6 µm
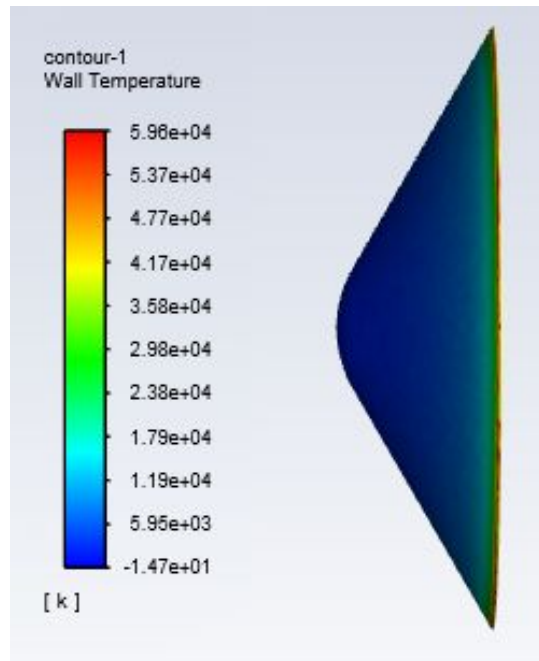
Figure 2.28 - Contour of 60 degree nose cone w/ surface roughness of 10 μm

4. Discussion

4.1   Reda vs base model CFD

Comparing Figures 2.16 and 2.19, a design difference should be noted between Reda's design and the actual design used for the project simulations. Reda's design was only rough at the tip of the nose cone, while for CFD the roughness affected all surfaces except for the back end. Taking this into account, looking at the wall temperature data range, it can be seen that results are within expected parameters. In Figure 2.16, the range is 550 to 900 K while for Figure 2.19 it is at 3300 to 22200 K.

There are many reasons to account for the margin error between the project simulation results and Reda's result. The most probable reason is that the exact material used for the CFD didn't match the one used for Reda's test. Reda stated that his nose cone was steel, but didn't state what grade of steel. As for the CFD, the simulation was further limited by the lack of grade choices for steel. With each grade of steel having its own thermal properties, this would explain the discrepancy.

Another factor to consider would be the viscous model used for calculation during the iteration. Since the nose cone was run through a wind tunnel, there was no base model to consider when running for the viscous model. The k-epsilon turbulence viscous model was chosen for the CFD, which played a major role in thermal data. This is due in part to how viscosity plays a role in how thermal energy is generated. In this case however, the viscous model may have produced too much turbulence leading to higher wall temperature values.

The final reason to consider would be user input error. With the basis of Reda's report being a wind tunnel experiment, conditions for the CFD had to be assumed, stated in the setup section. Assumptions were used to determine the mesh, the flow conditions, and the number of iterations completed for each case simulation. Though there was no real similarity between Reda's and this project's simulations, there was consistency for the CFD nose cone comparison

4.2   CFD nose cone comparison

4.2.1   Surface roughness

Analyzing the CFD simulations in Figures 2.17 - 2.28, it is apparent how the change in surface roughness and nose cone angle affects the location of the transient point of the surface of the various nose cones. Giving a general analysis, looking at the figures, as the surface roughness

increases, the transient point moves upstream of the flow. To explain, increased surface roughness means increased temperature, and in most cases means that the transient point occurred at an earlier position along the nose cone, allowing time for the additional heat. Since there is no distinct measuring device in ANSYS to measure the location of the transient point, there will be heavy reliance upon the surface color scheme. The transient point should be where there is a rapid change in temperature. An example is in Figure 2.18 where it jumps from a dark blue to light blue without a transitioning phase is apparent.

When the surface roughness increases in depth, the amount of turbulence increases causing min and max temperatures to increase. An example of this being evident is when the nose cone is at a 30 degree angle. At around 0 μm, the wall temperature max is at about 19,000 K. It then pops up to around 20,000 when the surface roughness is at 3 μm and 5.6 μm. At the deepest surface roughness of 10 μm, the max wall temp. was at 25,000K. Be aware, that these max temps do not reflect realistic conditions in an everyday scenario as the max temperature of steel is around 1100 to 1400 K. It is only viable for these case simulations because the high temps don't account for a huge surface area of the cones, thus can be considered a marginalized error.

4.2.2   Nose cone angle

When comparing the wall temperatures of the CFD figures, it was determined that as the angle of the nose cone increases, so does the temperature. An unexpected anomaly found was that with the angle increase also came a bigger temperature range, expanding into lower and higher number values. In one case for Figure 2.28, the cone had a lower range end of -1.47 K. Though this is still a viable temperature for the cone material, it should be considered neglected due to its abnormal value as well as simplify the simulation data results.

Looking at the 5.6 μm surface roughness of the 30, 45, and 60 degrees nose cones, a common pattern can be seen. First taking a look at the 30 degree nose cone, we have a max 22000 K. It then jumps to 28000 K for the 45 degrees nose cone, and then to 41000 K for the 60 degrees nose cone. An unexpected outcome however when looking at the angle sets separately is that when the angle increased, it appears that the point of transience seems to have shifted downstream.

4.2.3   Transient point

Finding the point where laminar turns into turbulent flow was difficult to measure using ANSYS due to program limitations. To compensate for this, determining the transient point was done by analyzing the temperature changes and determining where the point would be most likely using aerodynamic assumptions such as shock wave principles in regards to static properties as well as flow properties.

As stated before in sections 4.2.1 and 4.2.2, the transient point location was affected by the change in surface roughness and nose cone angle. When comparing the individual cases for each angle set, it can be seen how the transient point moves with the increase of surface roughness. These were expected results with the increase of turbulence and thus temperature due to less surface smoothness. Unexpected results presented were when comparing the angle sets to another. As stated previously, as the nose cone angle increased, the transient point also increased. This shouldn't have happened according to aerodynamics theory. With a bigger angle deflection from the mainstream, the transition to turbulence should have occurred more upstream. Though there is a temperature rise with each angle increase, it doesn't line up with where the transient point should be located. In short, it supports the idea of the nose cone angle on transient point location but not with the expected outcome.

5. Conclusion

With manufacturing companies turning away from traditional methods of manufacturing, metal parts are being made by means of 3D printing. Using the "layering" method to either build or cut a design into reality, it is soon becoming a faster and more cost-effective method of production. But with any type of manufacturing, there will always be levels of surface roughness affecting the aerodynamics of the object. One such case is the location of the transient point where laminar flow transitions into turbulent flow. Taking Reda's "*Transition Experiments on Large Bluntness Cones with Distributed Roughness in Hypersonic Flight*" as a base for the project, simulations were done comparing how surface roughness as well nose cone angle affected the transient point location. After 12 cases were run with surface roughness values of 0, 3, 5.6, and 1 μm at angles of 30, 45, and 60, the results were not something expected. Compared to the base model, the simulations had higher temperature values. And as for the actual simulation sets, with each roughness increase, the transient point moved upstream but it was the opposite when it came to angle increase. There are many possible reasons for these anomalies as was in section 4. However, the project and simulations were successful in displaying how the nose cone condition can affect the transient point location.

6. Future work

Proceeding from here, there are many possible experiments and studies that can be built off of this project. There can even be improvements made to the current project to obtain better results.

Starting with the current project, due to time and program limitations, the course of the study was not extracted to its full potential. In redoing the CFD, it should be run for a longer time frame with a higher element count. In addition, it would be beneficial to find software that can find more data options such as the transient point locator which was not possible with ANSYS. If ANSYS is still to be used, adjustments to the mesh and solver conditions should be made to get more fine-tuned results that match theoretical ideas.

Turning away from what can be corrected, there are many spin-off experiments and studies that can be built off of this project. The simplest one would be to test out more nose cone angles and surface roughness depths. But it can go even further, for example changing the material of the nose cone. The test conditions can also be adjusted; the viscous model can be changed to a different type, the speed and density of the airflow can be altered, even the shape of the nose cone itself can be messed with. All of these would help develop a better idea of how different nose cones can affect performance.

References

[1]   Franklin, J., "The Ultimate Guide to Understanding 3D Printer Accuracy,"
EnvisionTEC. August 24, 2017.
Available:https://envisiontec.com/understanding-3d-printer-accuracy/.

[2]   Simpson, T. W., "Understanding Surface Finish of Metal 3D-Printed Parts," *Additive
Manufacturing Magazine*. October, 2018.
Available:https://www.additivemanufacturing.media/blog/post/understanding-surface-fini
sh-of-metal-3d-printed-parts.

[3]   The Editors of Encyclopaedia Britannica, "Turbulent flow," *Encyclopædia Britannica*,
2017
Available:https://www.britannica.com/science/turbulent-flow.

[4]   Gradl, Paul, et al. "AIAA Joint Propulsion Conference." AIAA Joint Propulsion
Conference. 9 July 2018,
https://ntrs.nasa.gov/archive/nasa/casi.ntrs.nasa.gov/20180006357.pdf.

[5]   Bournias-Varotsis, A., Friel, R. J., Harris, R. A., and Engstrøm, D. S., "Ultrasonic
Additive Manufacturing as a form-then-bond process for embedding electronic circuitry
into a metal matrix," Journal of Manufacturing Processes, vol. 32, 2018, pp. 664–675.

[6]   "Friction Stir Additive Manufacturing Used for Functionally Graded Components -
3DPrint.com: The Voice of 3D Printing / Additive Manufacturing," 3DPrint.com | The
Voice of 3D Printing / Additive Manufacturing. May, 2017.
Available: https://3dprint.com/174645/friction-stir-am/.

[7]   "Cold Spray Forming for Additive Manufacturing," Cold Spray | TWI Additive
Manufacturing Available:
http://www.twiadditivemanufacturing.com/capabilities/metal-processing/cold-spray/.

[8]   Gradl, P. R., Protz, C. S., and Wammen, T., "Additive Manufacturing and Hot-fire
Testing of Liquid Rocket Channel Wall Nozzles Using Blown Powder Directed Energy
Deposition Inconel 625 and JBK-75 Alloys," AIAA Propulsion and Energy 2019 Forum,
2019.

[9]   "Surface Roughness," Surface Roughness Produced by Common Production Methods - Buford, GA - CAB Incorporated
Available: https://www.cabinc.com/toolkit/surface-roughness.

[10]   Radespiel, R., Ali, S. R. C., Muñoz, F., Bowersox, R., Leidy, A., Tanno, H., Kirk, L. C., and Reshotko, E., "Experimental Investigation of Roughness Effects on Transition on Blunt Spherical Capsule Shapes," Journal of Spacecraft and Rockets, vol. 56, 2019, pp. 405–420.

[11]   Varma, A. S., Sathyanarayana, G. S., and J, S., "CFD Analysis of Various Nose Profiles," International Journal of Aerospace and Mechanical Engineering, vol. 3, Jun. 2016.

[12]   Classification of Flows, Laminar and Turbulent Flows. 2005.
Available:http://www-mdp.eng.cam.ac.uk/web/library/enginfo/aerothermal_dvd_only/aero/fprops/pipeflow/node8.html.

[13]   Reda, D., Wilder, M., and Prabhu, D., "Transition Experiments on Large Bluntness Cones with Distributed Roughness in Hypersonic Flight," 50th AIAA Aerospace Sciences Meeting including the New Horizons Forum and Aerospace Exposition, Sep. 2012.

[14]   "Oblique Shock Waves," *NASA*. June, 2014
Available: https://www.grc.nasa.gov/WWW/BGH/oblique.html.

[15]   "Centered Expansion Fan," *NASA*. Apr, 2018.
Available: https://www.grc.nasa.gov/www/k-12/airplane/expans.html.

[16]   "Which is better in a heat transfer, laminar flow or turbulent flow?," Quora. Mar, 2017.
Available:https://www.quora.com/Which-is-better-in-a-heat-transfer-laminar-flow-or-turbulent-flow.

[17]   Hollis, B. R., "Experimental Investigation of Roughness Effects on Transition Onset and Turbulent Heating Augmentation on a Hemisphere at Mach 6 and Mach 10.," 2017.

[18]   Hosch, W. L., "Navier-Stokes equation," Encyclopædia Britannica, 2018.
Available: https://www.britannica.com/science/Navier-Stokes-equation.

[19]   "Navier-Stokes Equation - ppt video online download," 2015.
SlidePlayer Available: https://slideplayer.com/slide/3837289/.

[20]   Anderson, J. D., Fundamentals of aerodynamics, Boston, NY: Mc-Graw Hill, 2001.

[21]   "K-epsilon turbulence model," Wikipedia. Nov, 2019.
        Available: https://en.wikipedia.org/wiki/K-epsilon_turbulence_model.

[22]   NOSE CONES EQUATIONS. 2010.
        Available: http://www.rimworld.com/nassarocketry/fabrication/nosecones/design.ht
        ml.

Appendices

Appendix A: CFD solver conditions for 30 degree nose cone with 0 roughness

```
Fluent
Version: 3d, dp, pbns, rke, transient (3d, double precision, pressure-based, realizable k-epsilon, transient)
Release: 19.5.0
Title:


Models
------

   Model                       Settings
   ----------------------------------------------------------------
   Space                       3D
   Time                        Unsteady, 2nd-Order Implicit
   Viscous                     Realizable k-epsilon turbulence model
   Wall Treatment              Standard Wall Functions
   Heat Transfer               Enabled
   Solidification and Melting  Disabled
   Radiation                   None
   Species                     Disabled
   Coupled Dispersed Phase     Disabled
   NOx Pollutants              Disabled
   SOx Pollutants              Disabled
   Soot                        Disabled
   Mercury Pollutants          Disabled
   Structure                   Disabled


Material Properties
-------------------

   Material: steel (solid)

      Property              Units    Method    Value(s)
      --------------------------------------------------
      Density               kg/m3    constant   8030
      Cp (Specific Heat)    j/kg-k   constant   502.48
      Thermal Conductivity  w/m-k    constant   16.27

   Material: air (fluid)

      Property                        Units    Method    Value(s)
      -------------------------------------------------------------
      Density                         kg/m3    constant  1.225
      Cp (Specific Heat)              j/kg-k   constant  1006.43
      Thermal Conductivity            w/m-k    constant  0.0242
      Viscosity                       kg/m-s   constant  1.7894e-05
      Molecular Weight                kg/kmol  constant  28.966
      Thermal Expansion Coefficient   1/k      constant  0
      Speed of Sound                  m/s      none      #f

   Material: aluminum (solid)

      Property              Units    Method    Value(s)
      --------------------------------------------------
      Density               kg/m3    constant   2719
      Cp (Specific Heat)    j/kg-k   constant   871
      Thermal Conductivity  w/m-k    constant   202.4


Cell Zone Conditions
--------------------

   Zones

      name          id   type
      -------------------------
      fff-1_solid1  3    solid
      fluiddomain   6    fluid
```

```
   Setup Conditions

      fff-1_solid1

         Condition        Value
         --------------------
         Frame Motion?    no
         Mesh Motion?     no

      fluiddomain

         Condition        Value
         --------------------
         Frame Motion?    no
         Mesh Motion?     no


Boundary Conditions
-------------------

   Zones

      name                 id   type
      -----------------------------------------
      wall-5-shadow        14   wall
      wall-5               5    wall
      wall-13              13   wall
      wall-12              12   wall
      inlet                7    velocity-inlet
      outlet               8    pressure-outlet
      walls                9    wall
      contact_region-src   10   interface
      contact_region-trg   11   interface

   Setup Conditions

      wall-5-shadow

         Condition                 Value
         -----------------------------------
         Material Name             aluminum
         Thermal BC Type           1
         Wall Motion               0
         Shear Boundary Condition  0
         Wall Roughness Constant   0

      wall-5

         Condition        Value
         -------------------------
         Material Name    aluminum
         Thermal BC Type  1

      wall-13

         Condition                 Value
         -----------------------------------
         Material Name             aluminum
         Thermal BC Type           1
         Wall Motion               0
         Shear Boundary Condition  0
         Wall Roughness Constant   0

      wall-12

         Condition        Value
         -------------------------
         Material Name    aluminum
```

44

```
         Thermal BC Type    1

      inlet

         Condition                 Value
         --------------------------------
         Reference Frame           1
         Velocity Magnitude (m/s)  3430

      outlet

         Condition    Value
         -----------------

      walls

         Condition                 Value
         ------------------------------------
         Material Name             aluminum
         Thermal BC Type           1
         Wall Motion               0
         Shear Boundary Condition  0
         Wall Roughness Constant   0

      contact_region-src

         Condition    Value
         -----------------

      contact_region-trg

         Condition    Value
         -----------------


Solver Settings
---------------

   Equations

      Equation      Solved
      -------------------
      Flow          yes
      Turbulence    yes
      Energy        yes

   Numerics

      Numeric                      Enabled
      --------------------------------------
      Absolute Velocity Formulation   no

   Unsteady Calculation Parameters


      ----------------------------------------------
      Time Step (s)                 6.2150181e-08
      Max. Iterations Per Time Step  50

   Relaxation

      Variable                  Relaxation Factor
      --------------------------------------------
      Pressure                  0.3
      Density                   1
      Body Forces               1
      Momentum                  0.7
      Turbulent Kinetic Energy  0.8
      Turbulent Dissipation Rate  0.8
```

45

```
    Turbulent Viscosity           1
    Energy                        1

  Linear Solver

                                  Solver    Termination  Residual Reduction
    Variable                      Type      Criterion    Tolerance
    ------------------------------------------------------------------------
    Pressure                      V-Cycle   0.1
    X-Momentum                    Flexible  0.1          0.7
    Y-Momentum                    Flexible  0.1          0.7
    Z-Momentum                    Flexible  0.1          0.7
    Turbulent Kinetic Energy      Flexible  0.1          0.7
    Turbulent Dissipation Rate    Flexible  0.1          0.7
    Energy                        F-Cycle   0.1

  Pressure-Velocity Coupling

    Parameter    Value
    ------------------
    Type         SIMPLE

  Discretization Scheme

    Variable                      Scheme
    -----------------------------------------------
    Pressure                      Body Force Weighted
    Momentum                      Second Order Upwind
    Turbulent Kinetic Energy      Second Order Upwind
    Turbulent Dissipation Rate    Second Order Upwind
    Energy                        Second Order Upwind

  Solution Limits

    Quantity                      Limit
    -------------------------------------
    Minimum Absolute Pressure     1
    Maximum Absolute Pressure     5e+10
    Minimum Temperature           1
    Maximum Temperature           5000
    Minimum Turb. Kinetic Energy  1e-14
    Minimum Turb. Dissipation Rate 1e-20
    Maximum Turb. Viscosity Ratio 100000
```